



Six years of mesospheric CO estimated from ground-based frequency-switched microwave radiometry at 57° N compared with satellite instruments

P. Forkman¹, O. M. Christensen¹, P. Eriksson¹, J. Urban¹, and B. Funke²

¹Department of Earth and Space Sciences, Chalmers University of Technology, Sweden

²Instituto de Astrofísica de Andalucía (CSIC), Spain

Correspondence to: P. Forkman (peter.forkman@chalmers.se)

Received: 29 March 2012 – Published in Atmos. Meas. Tech. Discuss.: 1 June 2012

Revised: 29 October 2012 – Accepted: 31 October 2012 – Published: 20 November 2012

Abstract. Measurements of mesospheric carbon monoxide, CO, provide important information about the dynamics in the mesosphere region since CO has a long lifetime at these altitudes. Ground-based measurements of mesospheric CO made at the Onsala Space Observatory, OSO, (57° N, 12° E) are presented. The dataset covers the period 2002–2008 and is hence uniquely long for ground-based observations. The simple and stable 115 GHz frequency-switched radiometer, calibration method, retrieval procedure and error characterization are described. A comparison between our measurements and co-located CO measurements from the satellite sensors ACE-FTS on Scisat (v2.2), MLS on Aura (v3-3), MIPAS on Envisat (V3O_CO_12 + 13 and V4O_CO_200) and SMR on Odin (v225 and v021) is carried out. Our instrument, OSO, and the four satellite instruments show the same general variation of the vertical distribution of mesospheric CO in both the annual cycle and in shorter time period events, with high CO mixing ratios during winter and very low amounts during summer in the observed 55–100 km altitude range. During 2004–2008 the agreement of the OSO instrument and the satellite sensors ACE-FTS, MLS and MIPAS (200) is good in the altitude range 55–70 km. Above 70 km, OSO shows up to 25 % higher CO column values compared to both ACE and MLS. For the time period 2002–2004, CO from MIPAS (12 + 13) is up to 50 % lower than OSO between 55 and 70 km. Mesospheric CO from the two versions of SMR deviates up to ± 65 % when compared to OSO, but the analysis is based on only a few co-locations.

1 Introduction

Above the tropopause, CO is formed in the upper mesosphere/thermosphere mainly by photo-dissociation of CO₂ and the major sink is by reactions with hydroxyl, OH. The vertical volume mixing ratio of middle atmospheric CO is characterized by low values in the stratosphere and a steep vertical gradient in the mesosphere.

The dynamics of the mesosphere is characterized by a seasonally varying global circulation, driven by the meridional temperature gradient, and the breaking of upwelling gravity waves. This global circulation brings down constituents from the upper mesosphere to the lower regions of the mesosphere and further down to the stratosphere at the winter pole region, and the reverse is seen at the summer pole region. Due to its long lifetime (weeks) in the mesosphere, CO is an excellent tracer of mesospheric dynamics, especially at high latitudes where both horizontal motions (e.g. caused by the meandering polar vortex) and vertical motion (e.g. caused by the global circulation) can be studied. Lopez-Puertas et al. (2000) surveyed CO observations and model simulations and showed that the CO abundance undergoes an annual cycle in the high latitude mesosphere and lower thermosphere region, with high values in the winter and low values in the summer. During the last 35 yr, middle atmospheric CO has periodically been observed from a variety of ground-based stations. Waters et al. (1976) was the pioneer in observing the rotational transition of CO at 115 GHz. Clancy et al. (1984) and Bevilacqua et al. (1985) made ground-based microwave observations of the seasonal variation of mesospheric CO. Aellig et al. (1995) made 115 GHz observations

and attributed variations in the CO column density to breaking wave activity in the mesosphere. de Zafra and Muscari (2004) used 230 GHz observations of CO as a tracer of polar mesospheric dynamics. Kasai et al. (2005) made the first CO observations using ground-based solar absorption infrared spectroscopy, Velazco et al. (2007) made a long record of strato-mesospheric CO column values using the same technique. Long-term CO measurements at both 115 GHz (Forkman et al., 2003b) and infrared wavelengths (Borsdorff and Sussmann, 2009) have been compared with data from the Whole Atmosphere Community Climate Model, WACCM. Forkman et al. (2005) used CO measurements to estimate the vertical motion of the global circulation. Burrows et al. (2007) estimated horizontal mesospheric winds at Antarctica by the Doppler shift of ground-based microwave CO measurements. Hoffmann et al. (2011) compared ground-based CO measurements at 230 GHz with different satellite sensors.

The Improved Stratospheric and Mesospheric Sounder (ISAMS) onboard the Upper Atmosphere Research Satellite (UARS) made the first global stratospheric and lower mesospheric CO measurements during 6 months in 1991–1992 (Allen et al., 1999). During the last ten years, several different satellite sensors have been observing mesospheric CO including the microwave limb sounders SMR/Odin (Dupuy et al., 2004) and MLS/Aura (Pumphrey et al., 2007), the sun tracking ACE-FTS/Scisat-1 (Clerbaux et al., 2008) and the infrared limb sounder MIPAS/Envisat (Funke et al., 2009).

The lowest rotational transition of CO is at 115 GHz. The advantage of observing at 115 GHz compared to higher frequency transitions is both that the troposphere is optically thinner at lower frequencies and that pressure broadening exceeds Doppler broadening up to about 70 km altitude, making it possible to estimate vertical profiles of CO up to this altitude and column values above.

Dicke-switching, i.e. signal-reference switching of the receiver, is the standard microwave observation method in order to reduce the effect of gain drift in the receiver system. The intensities of the signal (the sky) and the reference (normally a blackbody load) have to balance each other to neutralize system gain nonlinearities. Frequency-switching, a small shift in the local oscillator frequency between the signal and reference phases, is a Dicke-switching variant. This method is mainly useful for the study of narrow lines like mesospheric CO at 115 GHz. One of the advantages of frequency-switching is that the line is present in both the signal and the reference phases, which doubles the effective observation time compared to “load-switching” where the reference is a blackbody load. The frequency-switching observing technique is commonly used in radio astronomy but more seldom used in microwave remote sensing.

In this study we present ground-based, frequency-switched measurements of mesospheric CO made at the Onsala Space Observatory, OSO, (57.4° N, 11.9° E). This is the longest ground-based measurement series of mesospheric

CO and covers the period 2002–2008. The instrument, calibration and inversion methods are described and the results are compared with data from four satellite instruments. Section 2 introduces our frequency-switched receiver system, Sect. 3 describes the inversions, Sect. 4 presents our results, Sect. 5 covers the satellite comparisons, and Sect. 6 gives a summary and the conclusions.

2 Measurement

2.1 Instrument and observation technique

Microwave remote sensing permits resolved line measurements of pure rotational transitions, which are sufficiently optically thin to allow observations from the ground. These lines are pressure-broadened in the atmosphere, and therefore the measured shape of the spectrum contains information on the number density of the emitting constituent as a function of pressure. Information of the vertical distribution of the emitting constituent can be estimated using mathematical inversion techniques (see Sect. 3).

We present measurements of CO made by a spectral, frequency-switched, heterodyne receiver used for the CO $1 \rightarrow 0$ transition at 115.27120 GHz based on a cooled Schottky single-sideband mixer. A block diagram of the receiver is shown in Fig. 1 and technical specifications are given in Table 1. The spectrometer is a 2-bit autocorrelator with 20 MHz bandwidth and 800 delay channels giving a nominal resolution of 25 kHz.

In the frequency-switched radiometer, the local oscillator is tuned between the signal and reference measurements. The intensities of the signal and reference phases balances each other as long as the frequency throw is small (normally <10 MHz). If the frequency is switched, $\pm \Delta f$ the observed spectral feature will appear both as a negative and a positive peak separated by $2\Delta f$ in the spectra. Since we use $\Delta f = 4$ MHz in the frequency-switching we have 8 MHz between the peaks as seen in Fig. 2. If the observed spectral feature is narrower than $2\Delta f$ it will not be affected by the switching. Frequency-switching can be performed at high speed (5 Hz), which will remove faster gain variations than traditional load-switching.

2.2 Calibration

The sky emission increases with decreasing elevation due to the increasing path length through the atmosphere. At the same time, however, the tropospheric absorption increases and therefore also the system temperature of the receiver. At 115 GHz the troposphere is fairly opaque and model calculations show that elevation angles larger than 30° give the highest signal to system-temperature ratio (Forkman et al., 2003a). For practical reasons we have chosen an elevation angle of 90° but the zenith observation direction also

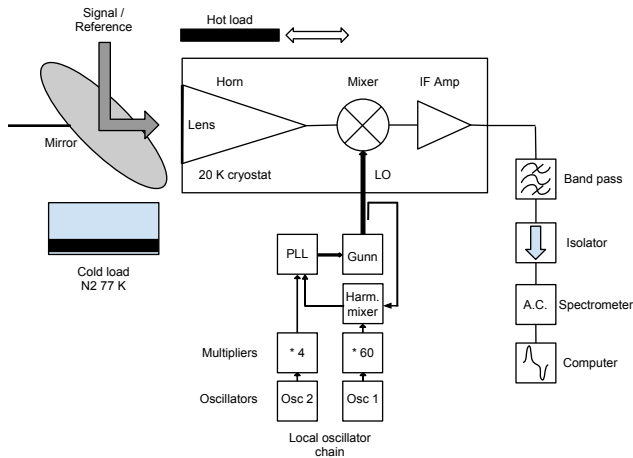


Fig. 1. Block diagram of the 115 GHz CO receiver system. The cold load is regularly mounted and used. Since the hot-cold calibrations are performed ahead of the lens, the losses in the lens and in the other components (horn, mixer, etc) along the transmission line are corrected for.

Table 1. Receiver specifications.

Radio frequency	115.261–115.281 GHz, SSB
Mirror edge taper	–35 dB
Elevation	90°, fixed
Cryostat window	Teflon lens
Horn	Aluminium, corrugated
Beam width, FWHM (lens included)	3°
First stage	Cooled Schottky mixer, 20 K
Image sideband rejection	Mechanical back short
Image sideband suppression	> 20 dB
Local oscillator (LO)	Gunn oscillator
LO frequency	111.27 GHz
Frequency throw ($2\Delta f$)	8 MHz
Mixer IF	4.0 ± 0.3 GHz
Total receiver temperature	~ 325 K
Backend spectrometer	800 channel autocorrelator
Bandwidth	20 MHz
Nominal resolution	25 kHz

minimizes Doppler shift effects due to horizontal movement of mesospheric air.

In microwave radiometry the intensity is normally presented as brightness temperature, T_b . The receiver output power is calibrated in units of antenna temperature, T_a . The antenna temperature is the sky brightness temperature distribution weighted with the antenna radiation pattern. Since the beam is quite narrow and the sky brightness temperature increases only slowly, when the elevation changes from zenith to lower elevations (Forkman et al., 2003a) the zenith pencil beam T_b can be well approximated with the measured T_a .

The net power reaching the spectrometer consists of two components. The first one is proportional to the sky

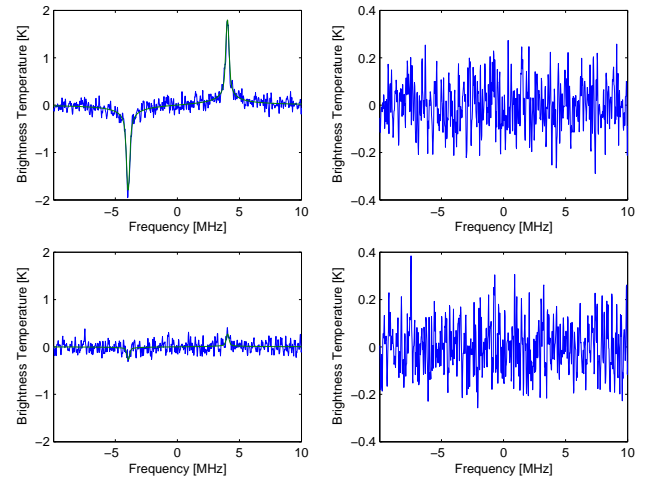


Fig. 2. To the left: measured spectra (4 h average) with retrieval fits. To the right: residuals (measured spectrum–fit). The frequencies are given relative to the CO line center. The negative and positive peaks are the result of the frequency throw in the frequency-switching method. The spectra are corrected for baseline features. Note the weak CO signal in the summer (bottom figures).

brightness temperature. The other component is the power generated in the receiver system (lens, horn, mixer, etc), which we identify as the receiver temperature, T_{rec} . The sum of these components is the system temperature, $T_{sys} = T_b + T_{rec}$.

To estimate T_{rec} , two blackbody loads with brightness temperatures T_{hot} (ambient load) and T_{cold} (77 K load) are observed each month. These hot-cold calibrations indicate that the variability of T_{rec} is less than 5 %.

Before each 15 min observation cycle, a calibration is performed to estimate the zenith sky brightness temperature. This is done by observing the zenith sky and an ambient load

$$\frac{P_{hot} - P_{sky}}{P_{sky}} = \frac{(T_{hot} + T_{rec}) - (T_b(z_0) + T_{rec})}{T_b(z_0) + T_{rec}}, \quad (1)$$

where P_{hot} and P_{sky} are the measured powers observing the hot load and the zenith sky respectively, $T_b(z_0)$ is the zenith sky brightness temperature (observed from the ground, z_0). $T_b(z_0)$ can be derived from the equation above since T_{hot} and T_{rec} are known.

Then during the observation cycle we record

$$\begin{aligned} \Delta T_b(z_0) &= T_b(z_0, f_+) - T_b(z_0, f_-) \\ &= \frac{\Delta P}{P_{hot} - P_{sky}} (T_{hot} - T_b(z_0)), \end{aligned} \quad (2)$$

where $\Delta T_b(z_0)$ is the difference in brightness temperatures between the two frequencies $f + \Delta f$ and $f - \Delta f$, ΔP is the difference between the measured powers at the two frequencies. P_{hot} , P_{sky} , T_{hot} and $T_b(z_0)$ are taken from the calibration.

2.3 The tropospheric correction

Assuming a 1-layer model for the troposphere, the microwave radiative transfer equation for a ground-based, zenith-looking observer can be written as

$$T_b(z_0) = T_b(z_{\text{trop}})e^{-\tau} + T_{\text{trop}}(1 - e^{-\tau}), \quad (3)$$

where $T_b(z_{\text{trop}})$ is the brightness temperature as observed from the tropopause, τ is the tropospheric zenith opacity and T_{trop} is the effective brightness temperature of the troposphere. If T_{trop} and τ are considered constant within the frequency throw we get

$$\Delta T_b(z_{\text{trop}}) = \frac{\Delta T_b(z_0)}{e^{-\tau}}. \quad (4)$$

In practice τ is calculated from Eq. (3) as

$$\tau = -\ln\left(\frac{T_{\text{trop}} - T_b(z_0)}{T_{\text{trop}} - T_{\text{bg}}}\right). \quad (5)$$

Since the atmospheric opacity is dominated by the contribution from the troposphere, the cosmic background radiation, T_{bg} , is used instead of $T_b(z_{\text{trop}})$ in Eq. (5). This means that the calculated τ actually is the atmospheric zenith opacity and hence includes the minor contribution from altitudes above the troposphere (e.g. absorption by stratospheric O₂ and H₂O).

The frequency-switching only yields $\Delta T_b(z_0)$, which is close to zero except for the line peaks. $T_b(z_0)$ therefore has to be measured separately as done in the calibration.

To be able to estimate T_{trop} in Eq. (5), one year of radiosonde data from the Gothenburg-Landvetter Airport (37 km north-east of the observatory) have been processed in forward model calculations (Forkman et al., 2003a). Our estimation of T_{trop} is based on the correlation between T_{trop} and the ground temperature, T_{gr} , but we include the sky brightness temperature, $T_b(z_0, \nu)$, to improve the estimate.

$$T_{\text{trop}}(\nu) = \alpha T_{\text{gr}} + \beta T_b(z_0, \nu), \quad (6)$$

where $\alpha = 0.89$ and $\beta = 0.10$ for $\nu = 115$ GHz are found by applying the method of least squares to the processed radiosonde data. The error of the T_{trop} estimate was found to be 3.5 K (1σ). Commonly T_{trop} is expressed as $0.95T_{\text{gr}}$, but the inclusion of $T_b(z_0)$ improves the estimate and reduces the error by 10 %.

2.4 Calibration errors

An error in the estimate of the receiver temperature, T_{rec} , affects the estimation of the sky brightness temperature, $T_b(z_0)$. If T_{rec} is within the observed variation the error in $T_b(z_0)$ should be less than 5 %. By comparing the thermal noise, σ_{tn} , in the measured spectra with theoretical calculations, an estimate of the systematic calibration error can be

found. σ_{tn} in the spectra can be estimated by fitting a polynomial to the measurement and calculating the standard deviations of the residuals. By using the *radiometric formula* a theoretical estimate of σ_{tn} is given by

$$\sigma_{\text{tn}} = \frac{K T_{\text{sys}}}{\sqrt{t \Delta \nu}}, \quad (7)$$

where t is the integration time, $\Delta \nu$ is the spectrometer resolution and K depends on the receiver type and configuration. In our case K reduces to 1.15, which corresponds to the loss of information due to the digitalization of the signal (van Vleck clipping correction), see Rohlfs and Wilson (2008) for further details. By comparing these two calculations of σ_{tn} we estimate the systematic error in $T_b(z_0)$ to be less than 5 %.

If the measurement and the tropospheric correction are made in one step (Eqs. 2 and 4) it is clearly seen that errors in the $T_b(z_0)$ estimation almost cancel out.

$$\Delta T_b(z_{\text{trop}}) = \frac{\Delta P}{P_{\text{hot}} - P_{\text{sky}}} (T_{\text{hot}} - T_b(z_0)) \frac{T_{\text{trop}} - T_{\text{bg}}}{T_{\text{trop}} - T_b(z_0)}. \quad (8)$$

The error in $\Delta T_b(z_{\text{trop}})$ due to calibration and the tropospheric correction is <2 %.

If T_{hot} and T_{trop} in Eq. (8) both are approximated with the ambient temperature, T_{amb} and $T_{\text{amb}} \gg T_{\text{bg}}$, we get

$$\Delta T_b(z_{\text{trop}}) = \frac{\Delta P}{P_{\text{hot}} - P_{\text{sky}}} T_{\text{amb}}, \quad (9)$$

which describes the ‘‘chopper wheel’’ calibration method, which can be used for a quick but not so accurate calibration and correction for the tropospheric attenuation in one step.

In total we believe that the systematic errors from the measurements and the tropospheric corrections, including the effect of the variability of the tropospheric opacity within the measurement cycles, are within 5 % across the used bandwidth.

3 Retrievals

3.1 Terminology

The inversions were done using the Optimal Estimation Method (OEM) (Rodgers, 2000). The state of the atmosphere and instrument are described by a *state vector*, \mathbf{x} . A *forward model*, \mathbf{f} , is then employed to map \mathbf{x} to a measurement, $\mathbf{y} = \mathbf{f}(\mathbf{x})$. The inverse problem consists in finding \mathbf{x} given some measurement \mathbf{y} . By linearizing the forward model $\mathbf{y} = \mathbf{K}\mathbf{x}$ around the a priori atmosphere (\mathbf{x}_a), where \mathbf{K} is the Jacobian or weighting function matrix ($\partial \mathbf{y} / \partial \mathbf{x}$), the problem can be solved using linear algebra.

Doing this and applying OEM, the best estimate of the state vector is

$$\begin{aligned} \hat{\mathbf{x}} &= \mathbf{x}_a + (\mathbf{K}^T \mathbf{S}_\epsilon^{-1} \mathbf{K} + \mathbf{S}_a^{-1})^{-1} \mathbf{K}^T \mathbf{S}_\epsilon^{-1} (\mathbf{y} - \mathbf{f}(\mathbf{x}_a)) \\ &= \mathbf{x}_a + \mathbf{G}_y (\mathbf{y} - \mathbf{f}(\mathbf{x}_a)), \end{aligned} \quad (10)$$

where \mathbf{S}_ϵ is the covariance matrix describing the uncertainty in the measurement, \mathbf{S}_a the covariance matrix for the a priori profile and \mathbf{G}_y the gain matrix. The relation between the true state, the a priori state and the retrieved state is given by

$$\hat{\mathbf{x}} - \mathbf{x} = (\mathbf{A} - \mathbf{I})(\mathbf{x} - \mathbf{x}_a) + \mathbf{G}_y \mathbf{K}_b (\mathbf{b} - \hat{\mathbf{b}}) + \mathbf{G}_y \Delta \mathbf{f}(\mathbf{x}, \mathbf{b}) + \mathbf{G}_y \boldsymbol{\epsilon}, \quad (11)$$

where \mathbf{A} is denoted the averaging kernel matrix, \mathbf{I} is the identity matrix, \mathbf{b} and $\hat{\mathbf{b}}$ the true and estimated value of forward model parameter (i.e. line strength), \mathbf{K}_b is the Jacobian matrix of the parameter ($\partial y / \partial \mathbf{b}$), $\Delta \mathbf{f}(\mathbf{x}, \mathbf{b})$ are errors in the forward model and $\boldsymbol{\epsilon}_x$ are errors in the measurement. For a complete definition and derivation see Rodgers (2000). The different terms will be discussed further in Sect. 4.1.

The AVK matrix is defined as $\mathbf{A} = \partial \hat{\mathbf{x}} / \partial \mathbf{x}$. It describes the sensitivity of the retrieval to a change in the true state. Each element \mathbf{A}_{ij} gives the change in the retrieved profile $\hat{\mathbf{x}}_i$, resulting from a perturbation in the true profile \mathbf{x}_j . A row in the AVK matrix can be regarded as a smoothing function (averaging kernel) describing the vertical resolution of the retrievals. The area of this smoothing function is called the *measurement response* and gives a rough indication of the contribution of the measurement to the retrieved value (Baron et al., 2002).

As mentioned in Hoffmann et al. (2011), the AVK will differ in shape depending on whether \mathbf{x} is representing the volume mixing ratio (VMR AVKs) or the relative change compared to the a priori concentration (fractional AVKs). Both type of AVKs will be presented in this paper for easier comparison with other studies, however we will mainly use the VMR AVKs to characterize the instrument.

3.2 Retrieval setup

For the OSO inversions the forward model was provided by ARTS (v2.0) (Eriksson et al., 2011), and the retrieval software is a new version of Qpack (v2.0) (Eriksson et al., 2005). The retrieved quantities are CO volume mixing ratios, temperature, instrumental baselines and a frequency shift in the instrument. Only the CO VMR will be presented as a retrieval product, whereas the three others are retrieved mainly to stabilize the retrieval process. To ensure that the frequency shift is compensated for, the inversions were performed in an iterative leap using a Marquardt-Levenberg algorithm (Marks and Rodgers, 1993).

The spectroscopic line strength and position were taken from the JPL 2001 database (Pickett et al., 1998), whereas the pressure- and self-broadening parameters as well as their temperature dependence coefficients were taken from the HITRAN 2000 database (Rothman et al., 2003). Some of the used CO spectroscopic data are given in Table 2. Since the absorption of O_2 and H_2O is compensated for in the tropospheric correction (see Sect. 2.3) the only line included in the forward model calculations was the CO line at 115.27 GHz.

Table 2. Some of the used CO spectroscopic data.

Center frequency, f_0	115.27120 GHz
Line intensity, I_0	$9.761128 \cdot 10^{-18} \text{ m}^2 \text{ Hz}^{-1}$
Air-broadened width	$23332.68 \text{ Hz Pa}^{-1}$
Self-broadened width	$25958.54 \text{ Hz Pa}^{-1}$
Reference temperature for broadening parameters	296 K
Temperature dependence exponent for broadening parameters	0.69

The retrieval was performed on a pressure grid ranging from 2738 Pa (~ 10 km) to 0.87 mPa (~ 130 km), with a logarithmic spacing of 0.125 decades (~ 2 km).

The temperature and pressure data were taken from the MSIS90 climatology (Hedin, 1991), and the temperature a priori covariance matrix was given as a matrix with diagonal entries $\mathbf{S}_{ii} = 25$ K (i.e. standard deviation of 5 K). Furthermore, since the temperature in the real atmosphere is correlated in altitude the non-diagonal elements $\mathbf{S}_{ij} = \sigma_i \sigma_j \rho_{ij}$ were constructed so that the correlation (ρ) would decline linearly with a correlation of 0.37 when the altitude difference (correlation length) between i and j was 4 km (roughly based on Eriksson, 2000).

The abundance of CO is highly variable over the year and OEM requires using the best estimate atmosphere as a priori. Therefore a monthly mean from a run of the Whole Atmosphere Community Climate Model (WACCM) (Garcia et al., 2007) was created and used as the a priori profile for the center day in each month. The value for other days were found by linearly interpolating onto each day. To simplify the error analysis, however, the covariance matrix for the a priori data was kept constant (in VMR) throughout the year.

Following Eriksson (2000), the covariance matrix for CO consists of two parts. The first represents the uncertainty of the mean a priori profile for each month. As with temperature, the covariance matrix must also represent correlation in altitude for this error. This was modeled to decline linearly with a correlation length of 8 km. The standard deviation was set to 50 % of the yearly mean of the a priori profiles. The second part represents the natural variability of CO on shorter timescales which was set to 0.5 ppm for all altitudes and with no correlation between the layers.

The OSO instrument had problems with baseline features before an upgrade on 7 January 2004. After this upgrade the baseline variation was reduced significantly. To account for this, an instrumental baseline was retrieved by fitting a 5th order polynomial with a diagonal a priori covariance matrix with entries from 20 K (0th order) to 5 K (5th order) for dates before this upgrade, and entries from 20 K (0th order) to 0.05 K (5th order) for dates after this upgrade. This leads to a different measurement response for the different dates.

Due to the performed Hanning windowing, the thermal noise in neighboring channels is correlated. The average

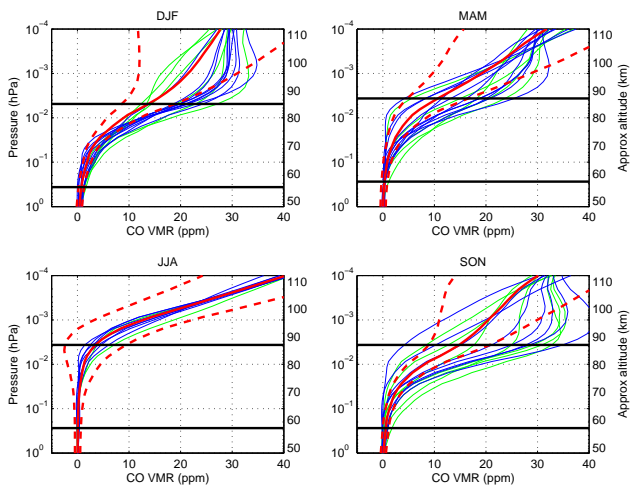


Fig. 3. Retrieved profiles 2002–2008 (every 20th profile is plotted for each season). CO volume mixing ratios are plotted against pressure (and altitude). The red line shows the average a priori profile for the season, and the dashed line the standard deviation of the a priori profile. Green lines are retrieved profiles 2002–2004 and the blue lines are profiles 2004–2008. The mean measurement response of the OSO instrument is higher than 0.8 between the black horizontal lines.

channel correlation of the thermal noise was measured to be 1.6 nominal channel widths, so S_ϵ was given as a covariance matrix with a correlation length of 1.6 nominal channel widths. The magnitude of the thermal noise was estimated in each measurement independently by fitting a polynomial of order 3 to the measurement and calculating the RMS of the residuals at the wings.

4 Results of the OSO measurements

Figure 2 shows a sample spectrum, the corresponding retrieved spectrum and the residuals for a typical winter and summer measurement. The CO line is much fainter during the summer than the winter line due to the strong seasonal cycle of CO (Sect. 1). The residuals are of equal strength, with both summer and winter showing that the system temperature is more or less constant during the year. Example profiles for each season are plotted in Fig. 3.

The shapes of the VMR AVKs are quite similar in both winter and summer. The most notable feature of the VMR AVKs is the negative values around 60 km for the AVKs corresponding to retrieved values above 90 km (pink and black curves in Figs. 4 and 5). Although this looks dramatic, it is important to remember that these AVKs represent the sensitivity to changes in VMR. The concentration of CO is much lower at 60 km than above 90 km, and accordingly the expected variability in CO VMR is also much lower. This implies that the impact of the negative lobes will be small, as the retrieved value follows the product of the AVK value and

the deviation from the a priori (see first term Eq. 11). The corresponding averaging kernels (the rows of AVK matrix) can be seen in Figs. 4 and 5.

Since CO has a very strong vertical gradient, relative changes at altitudes above the target altitude will give a larger effect than relative changes beneath. This changes the shape and area of the fractional AVKs, especially around 70 km during the summer where the fractional AVKs becomes extremely wide. Here strong vertical gradients combined with poor vertical resolution even results in the measurement response of the fractional AVKs to become greater than one. This means that a concentration change of 10 % at one altitude could give a responding change of 20 % at a lower altitude.

This complication is less prominent when using the VMR AVKs, rather than the fractional AVKs, to define the measurement response of the instrument. Note that the measurement response then describes the instruments' sensitivity to changes in vmr rather than changes relative to the a priori. The use of VMR AVKs is motivated by the fact that the strong vertical gradient of CO combined with a meandering vortex can lead to extremely large changes in the true atmosphere relative to the a priori. This variation is easier to describe in VMR rather than relative units, and the sensitive range is therefore given as such. To further address the issue of the poor vertical resolution above 70 km, only the column (rather than individual layers) will be used above this altitude.

The retrievals have an average degree of freedom (trace of the AVK matrix) of 1.8 before 2004 and 2.2 after 2004. The measurement response (VMR) is above 80 % approximately between 55 and 85 km. The vertical resolution within this altitude range is about 15–20 km (see Figs. 4 and 5). The beam of the OSO instrument has a horizontal width of about 4 km in the mesosphere.

The results presented in this paper will be given as the mixing ratios at 36 Pa (55 km), 12 Pa (63 km) and columns above 4 Pa (71 km) where Doppler broadening dominates. The column values are calculated by summing up the number densities from the air pressures below 4 Pa. The number densities are calculated from the retrieved profiles using the a priori temperature profiles.

4.1 Errors

The error of the retrieval is the difference between the true state x and the retrieved state \hat{x} . The error can be divided into several parts corresponding to each term in Eq. (11).

The first term is known as the *smoothing error* and represents the error at each altitude, which arises from the limited vertical resolution of the retrieval. When analyzing a profile from a given instrument this has to be taken into account, either by saying that the value at each altitude is the average represented by the AVK or by stating the smoothing error. In this study the averaging kernels of the OSO instrument

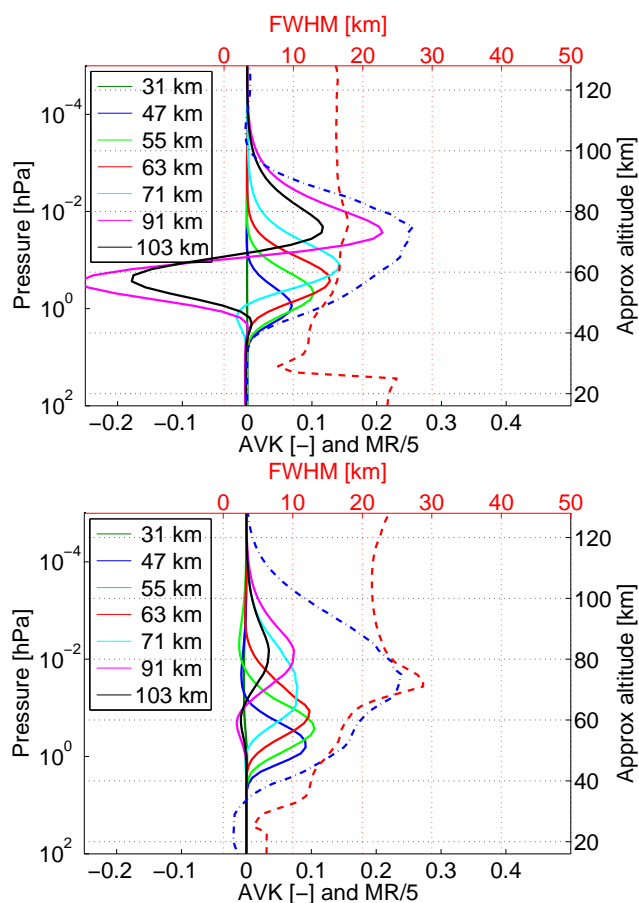


Fig. 4. Solid lines show the averaging kernels from 27 December 2005 in vmr (a) and fractional (b) units for different altitudes. The blue dash-dotted line is the measurement response divided by 5. The red dashed line shows the FWHM of the averaging kernels.

is taken into account by Eq. (12) and the smoothing error is thus ignored. The second term is the *model parameter error*, which describes the error in the retrieval arising from the difference between the true value of a forward model parameter \mathbf{b} and the estimated value $\hat{\mathbf{b}}$. This will be discussed further in Sect. 4.2. The third term is the *forward model error*, which comes from direct errors in the forward model from either approximations or not modeled processes. This last term will not be discussed in this paper and is negligible. A thorough validation of ARTS is presented in Melsheimer et al. (2005).

The last term is the *retrieval noise*, which is the error coming from noise in the measured spectra. It is described by the covariance matrix $\mathbf{S}_m = \mathbf{G}_y \mathbf{S}_e \mathbf{G}_y^T$. This error is random and will introduce noise into the retrieved profiles. An estimate of this noise is shown as the blue lines in Fig. 6. The dashed (dashed-dot) line shows the value for winter (summer) retrievals and the solid line the mean retrieval noise. The big difference between summer and winter values is due to the low concentration of CO during summer.

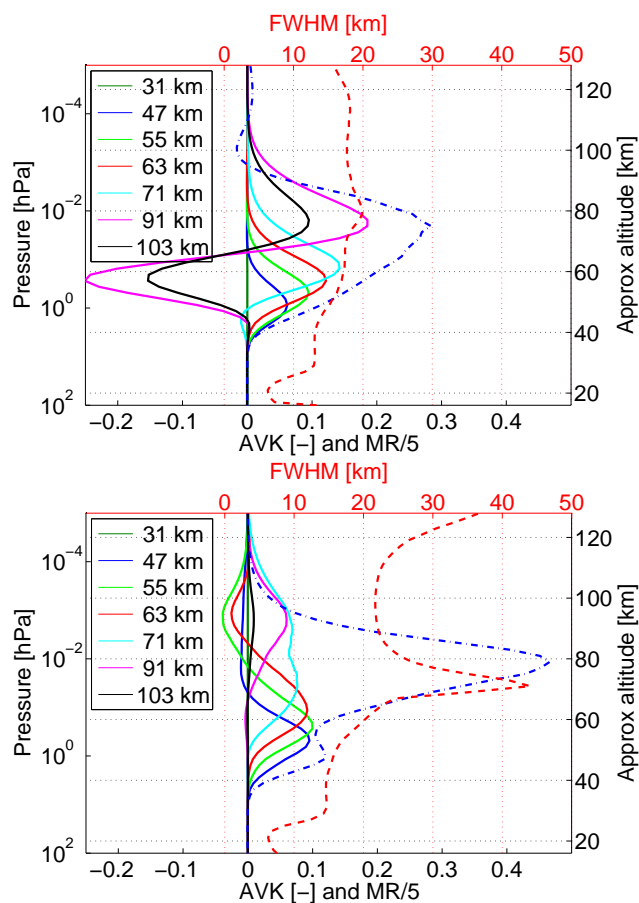


Fig. 5. Solid lines show the averaging kernels from 26 June 2006 in vmr (a) and fractional (b) units for different altitudes. The blue dash-dotted line is the measurement response divided by 5. The red dashed line shows the FWHM of the averaging kernels.

4.2 Forward model parameter errors

In addition to the errors accounted for in the retrieval, there will be systematic errors from the forward model as well as instrumental errors which might influence the retrievals. To estimate the influence of errors in different retrieval parameters on the results, the retrievals from year 2006 were used. The summer values (JJA) were removed resulting in 177 remaining spectra, which were rerun with the different parameters perturbed with their estimated 1σ -error. The differences between the standard and the perturbed inversions show that errors in forward model parameters can lead to a systematic error (bias) as well a decreased precision in each measurement. The systematic error can be described by $\mathbf{x}_{\text{pert}} = k \cdot \mathbf{x}_{\text{std}}$ at each altitude, where \mathbf{x}_{pert} is the value of the perturbed inversion, \mathbf{x}_{std} the retrieved value using the standard parameter values and k a coefficient which can be found by linear regression. The estimated relative error can then be expressed as $|100 \cdot (k - 1)| \%$ (Pumphrey et al., 2007). The decreased precision is estimated by the standard deviation of

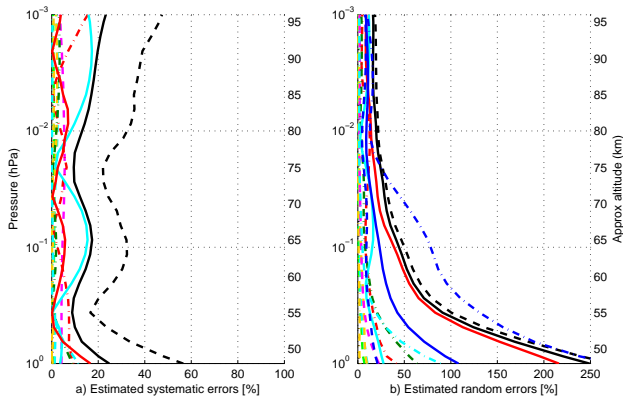


Fig. 6. In (a) the estimated systematic errors and in (b) the random errors. The colored (except blue) lines show the mean relative change (a) and standard deviation (b) in the retrieved value at each altitude as the different forward model parameters are perturbed. The forward model parameters are: line-strength, I_0 , (green-dashed), temperature profile, T , (cyan-dashed), pressure broadening parameter, γ_P , (yellow-dashed), temperature coefficient for the broadening parameter, α_P , (yellow-dashed-dot), a priori profile, x_a , (red-dashed-dot), 50 % a priori uncertainty, S_x , (green-dashed-dot), removing natural variability from a priori uncertainty, S_x , (red-solid), a priori uncertainty for the polynomial fit (cyan-dashed-dot), calibration errors (magenta-dashed-dot) and backend channel broadening error (cyan). The black line in both figures is the root-sum-square of the parameter errors. In (a) the black-dashed is the sum of the errors. The dark blue lines in (b) show the retrieval noise from 1 January 2006 (dashed), 2 September 2006 (dashed-dot) scaled with the a priori profile for the respective day as well as the average retrieval noise (solid). The black dashed line in (b) is the root-sum of the average retrieval noise (blue-solid) and the total parameter variability (black-solid).

the relative difference between the standard and perturbed inversions (i.e. scaled with the a priori).

The different forward model parameters tested include the line strength of the CO transition, the pressure broadening parameter and the instrument backend channel response. In addition, the a priori temperature profile, a priori CO profile, a priori uncertainty and size of the polynomial baseline fit were perturbed to test the possible systematic errors arising from different retrieval parameters.

For the spectral parameters the error estimates were done by comparing the values for HITRAN 2000, HITRAN 2008 and JPL 2001. If the discrepancies between the databases were bigger than the given error estimate in the database the discrepancy was used, if not the error estimate from the database was used. This gives a line strength I_0 uncertainty of 1 % (JPL-database), a pressure broadening parameter γ_P uncertainty of 10 % (HITRAN 2000 uncertainty) and an uncertainty in the temperature coefficient α_P of the pressure broadening parameter of 10 % (difference between HITRAN 2000 and HITRAN 2008). Errors in the self-broadening parameters were found to be insignificant to the retrieval and will

not be presented in this paper. In total, the spectroscopic parameters together give errors of less than 5 % in the retrievals.

To investigate the influence of the calibration errors, the spectra were simply multiplied with 1 ± 0.05 to simulate the 1σ calibration error (see Sect. 2.4). To test the influence of the a priori, the CO profile was perturbed by 50 % and the standard deviation for the a priori uncertainty covariance matrix was changed with 50 %. In addition, another test was done where the part representing the natural variability (0.5 ppm at all altitudes) was removed from the uncertainty matrix, and only the uncertainty in a priori mean was used. The temperature profile was perturbed by 5 K (1σ error for MSIS90 is 3 K) to take errors in temperature into account. The polynomial baseline fit in the retrieval had its a priori variance multiplied and divided by 4.

Figure 6a shows the estimated systematic error for the different parameters and their root-sum-square (solid black). This estimate indicates the total systematic error expected in the measurements. The solid black line shows the sum of all the errors, this represents a worst case scenario for systematic errors which we will use before 2004.

In addition to the systematic errors, uncertainties in the forward model and retrieval parameters also lead to a decreased precision. Figure 6b shows the standard deviation from each parameter and their root-sum-square (solid black). Combined (root-sum-square) with the average retrieval noise (blue solid) an estimate of the precision of the measurements is obtained and shown as the black dashed line in Fig. 6b.

The total estimated averaged systematic error between 55–85 km is in the order of 15 % for profiles and 10 % for column values. The worst case error, the sum of the different errors, is of the order of 25 % for profiles and 20 % for the column values. Estimated average random errors between 55–85 km is 30–50 %, but is significantly worse when the concentration of CO is low. The random errors mainly comes from the retrieval noise, and depend heavily on the a priori uncertainty at those altitudes (red curve Fig. 6), with a higher uncertainty leading to more noise. The retrieval noise from one such date (2 September 2006) is shown as the dashed-blue line in Fig. 6b.

5 Comparison

5.1 Satellite instruments

The four satellite instruments which observed mesospheric CO during the time period 2002–2008 are the sun tracking ACE-FTS on Scisat-1 (Clerbaux et al., 2008), the microwave limb sounder MLS on Aura (Pumphrey et al., 2007), the infrared limb sounder MIPAS on Envisat (Funke et al., 2009) and the microwave limb sounder SMR on Odin (Dupuy et al., 2004). The temporal and mesospheric vertical coverage are different for the four satellites. Table 3 gives the

Table 3. Satellite and data characteristics.

Satellite instrument	ACE-FTS	Aura-MLS
Reference	Clerbaux et al. (2008)	Pumphrey et al. (2007)
CO data version	V 2.2	V-3-3
Measurement principle	Sun tracking, absorption	Limb sounding, emission
Wavelength or frequency	2.3 & 4.7 μm	230 GHz
Launch	12 August 2003	15 July 2004
Orbit inclination	74°	90°
Vertical range	6–100 km	16–80 km
Vertical resolution (mesosphere)	4 km	7–8 km
Horizontal resolution (mesosphere)	500 km	200 km
Systematic errors (above 60 km)	Better than $\pm 25\%$	$\pm 20\%$
Co-location range satellite-OSO	< 1500 km & < $\pm 20\%$ PV	< 1500 km & < $\pm 20\%$ PV
Co-located measurement days	126	618
Satellite instrument	Envisat-MIPAS	Odin-SMR
Reference	Funke et al. (2009)	Dupuy et al. (2004)
CO data version	V3O(12 + 13) 2003–2004	V021 (new version)
CO data version	V4O(200) 2005–2008	V225 (old version)
Measurement principle	Limb sounding, emission	Limb sounding, emission
Wavelength or frequency	4.7 μm	576.4 GHz
Launch	1 March 2002	20 February 2001
Orbit inclination	98.6°	97.8°
Vertical range	6–70 km	17–110 km
Vertical resolution (mesosphere)	10 km	3 km
Horizontal resolution (mesosphere)	500 km	500 km
Systematic error (50–70 km)	$\pm 10\%$	Not available
Co-location range satellite-OSO	< 1500 km & < $\pm 20\%$ PV	< 1500 km & < $\pm 20\%$ PV
Co-located measurement days	418	22

characteristics of the four satellite sensors. As seen in Table 3, we use two different CO datasets for MIPAS and SMR. For MIPAS we use version V3O_CO_12 and V3O_CO_13 obtained from high spectral resolution measurements during 2003–2004 and version V4O_CO_200 in the period 2005–2008 when the MIPAS spectral resolution was reduced as consequence of an instrumental failure. All MIPAS observations used here were taken in the nominal observation mode covering tangent heights within 6–70 km. For SMR we use both the older v225 and the newer v021. V021 is an extended dataset compared to v225 using all the available observation modes. V225 has been used in previous comparisons (e.g. Clerbaux et al., 2008).

5.2 Comparison procedure

Side-looking satellites and a zenith-looking ground-based instrument do not observe the same air volume. Comparisons between satellite- and ground-based instruments are therefore complicated. All the satellites report data from a 100 times longer horizontal path than OSO but their vertical resolution are up to four times better. Differences in vertical resolution can be compensated for by using the averaging kernels of the instruments but differences in horizontal resolution are harder to adjust for. A second issue is the co-location criterion to apply. At periods when small horizontal variations of CO are expected in the mesosphere (as in the summer)

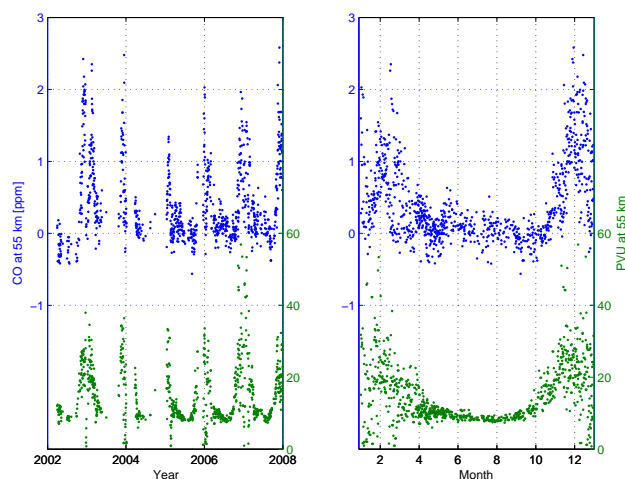


Fig. 7. CO volume mixing ratio and PV above OSO at 55 km altitude. To the left: the time series 2002–2008. To the right: the data from the different years stacked together. The modified Ertel's PV is used and $1 \text{ PVU} = 10^{-6} \text{ K m}^2 \text{ s}^{-1} \text{ kg}^{-1}$. The overall correlation between CO and PV is 0.63.

the air above OSO should be rather similar to air inside the co-location radius of 1500 km chosen in this study. A higher variability is expected in the wintertime when the movement of the polar vortex brings in or out CO rich air above the OSO instrument, and the concentration can vary substantially both

within 1500 km radius from OSO and along the horizontal paths of the satellite beams. These deviations can partly be compensated for by using observed potential vorticity as a supplementary co-location criteria.

The polar vortex builds up in the autumn and breaks down in the spring. The potential vorticity (PV) of an air parcel is a measure of the position of the air parcel relative to the polar vortex. Figure 7 shows the OSO CO volume mixing ratio at 55 km together with the modified Ertel's PV (Lait, 1994), calculated from the ECMWF operational dataset at 55 km during the time period 2002–2008. Figure 7 shows both a time series for the different years and the data for the different years stacked together to clearly see the seasonal variation. Both the CO mixing ratio and the PV have a steep and distinct increase in the autumn. The winter is characterized by the meandering of the polar vortex, which brings in or out CO rich air from the polar region and this causes fast variations of both CO mixing ratio and PV. The decrease in CO and PV in the spring is both less steep and less distinct than the increase in the autumn. The PV is low and stable in the summer and the CO mixing ratio is close to zero but show a high variability in the measurements. The high variability is explained by the faint CO signal in the summer which gives a low signal to noise ratio. The overall correlation between the CO mixing ratio and PV is 0.63.

The co-location criteria was chosen as follows: the temporal co-location criteria was set to the same date for satellite and OSO. The air volume measured by the satellite had to be within a radius of 1500 km from OSO. The potential vorticity (PV) of the air volume measured by the satellite had to be within 20 % of the PV above OSO (Hoffmann et al., 2011 used a similar co-location procedure). The PV data were taken from the ECMWF operational data set at the potential temperature level of 2000 K (~ 50 km altitude) and the modified Ertel's PV (Lait, 1994) was calculated for both satellites and OSO. Figure 8 show the co-located positions for the four satellites.

For the comparison, the satellite data were interpolated onto the OSO retrieval grid. In the relevant vertical range the best resolution of the different satellites are roughly 4 km, which is about twice the interpolation resolution used. Hence the interpolation errors should be small ($< 1\%$) which also is confirmed in a test (not shown).

For grid points outside the valid data points for the satellite the OSO a priori CO data were used. To take into account the different vertical resolution of the instruments the satellite data was convolved with the averaging kernels, A , of the OSO instrument (Rodgers and Connor, 2003)

$$\mathbf{x}_s = \mathbf{x}_a + \mathbf{A}(\mathbf{x}_{\text{sat}} - \mathbf{x}_a), \quad (12)$$

where \mathbf{x}_s is the smoothed version of the satellite profile \mathbf{x}_{sat} , and \mathbf{x}_a is the OSO a priori profile.

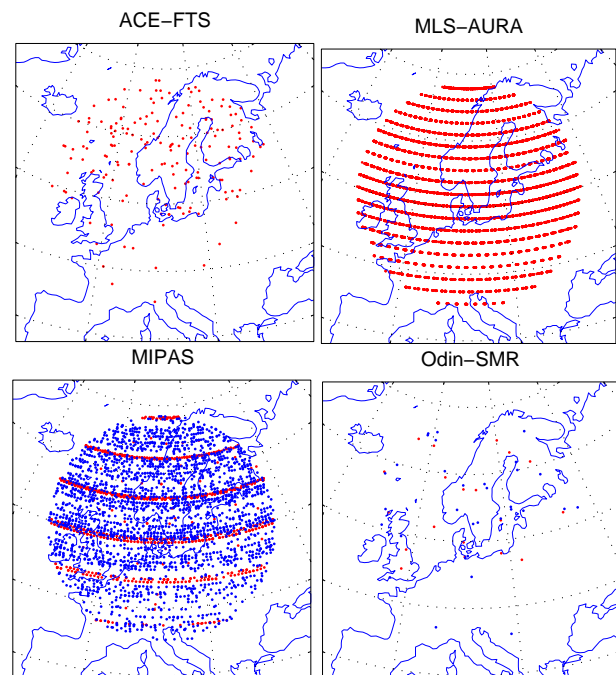


Fig. 8. Satellite (co-location) positions. The dots indicate the satellite positions within 1500 km radius from OSO, which also fulfill the PV criteria. In the MIPAS co-location map red/blue dots show (12 + 13)/(200) data, respectively. In the Odin co-location map red/blue show v225/v021, respectively.

5.3 Results of the satellite comparison

The satellite comparison is divided in the time periods: 2002–2004 and 2004–2008. As mentioned in Sect. 3.2 there were baseline features in the OSO spectra 2002–2004 that may have affected the retrieved vertical profiles. These features disappeared when the local oscillator chain of the instrument was rebuilt in the beginning of 2004. Figure 9 shows time series of CO from OSO, MIPAS (12 + 13) and SMR (021 + 225) for the time period 2002–2004 and Fig. 10 show time series from OSO, ACE, MIPAS (200), MLS and SMR (225) for the time period 2004–2008. Both figures show CO volume mixing ratios at 55 and 63 km and column values above 71 km. No column values are presented for MIPAS and MLS since the nominal MIPAS CO observations are not vertically resolved above 70 km, and the upper limit for MLS is about 80 km. Figure 11 shows the WACCM mean CO volume mixing ratio and the mean CO number densities. The main contribution for the column values is from altitudes < 100 km, even if the volume mixing ratio is increasing with altitude. This is explained by the exponential decrease in air pressure, and hence in air density, with altitude.

As seen in Figs. 9–10 all instruments show the same general features in both the annual cycle and in sporadic events. The noticeable difference between OSO and the satellites in

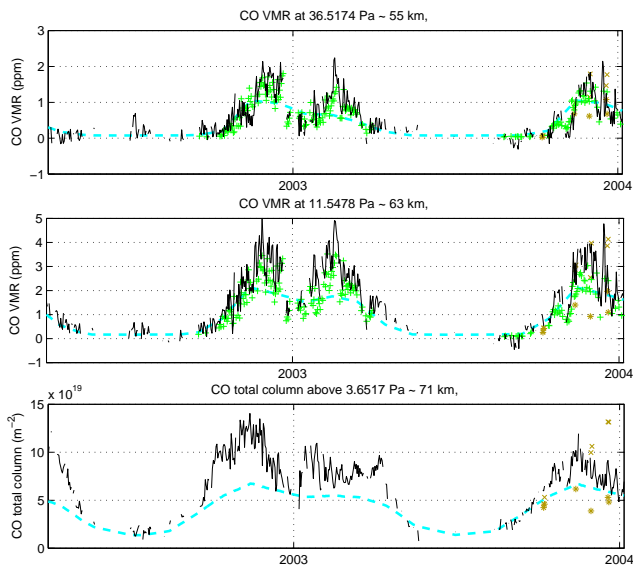


Fig. 9. Time series of CO mixing ratio at 55 km and 63 km and columns above 71 km for the time period 2002–2004 are shown: OSO (black), MIPAS (12 + 13, green plus), SMR (V021, brown cross; V225, brown stars) and a priori (cyan).

these figures is mainly the higher values of OSO compared to MIPAS (12 + 13) at 63 km (Fig. 9).

Figures 12–13 and Table 4 give a more detailed view of the comparison. Figure 12 shows the mean relative differences between the satellites and OSO for the time periods 2002–2004 and 2004–2008. The differences are discussed for each satellite instrument later in this section.

Figure 13 shows the mean absolute and relative standard deviations between OSO and the satellites. These deviations originate from noise in the different instruments, from fluctuations due to insufficient co-location and forward model/retrieval parameters. Below 65 km the OSO measurement response gradually decreases, which explain the increase of the deviations below this altitude.

Table 4 gives a supplement to Figs. 12–13 showing the mean relative differences, the mean standard deviations and the mean correlation between OSO and the satellites. The correlation of the data from OSO and the satellite instruments is high.

The OSO summer CO spectra have a very low signal to noise ratio leading to a higher relative noise (Figs. 2b and 6). This gives a high variability in the retrieved summer mixing ratios (Fig. 10). The summer values are therefore excluded in Figs. 12–13 and Table 4 to avoid the noisy OSO summer measurements interference in the satellite comparison.

Taken into account the systematics errors of OSO ($\leq 15\%$) and the satellites (20–30%, see Table 3) OSO overlaps the satellites in the time period 2004–2008 when OSO is compared to ACE, MIPAS (200) and MLS.

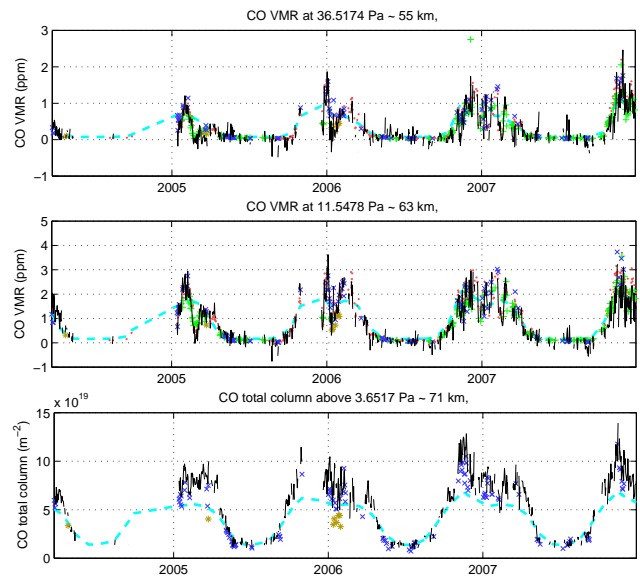


Fig. 10. Time series of CO mixing ratio at 55 km and 63 km and columns above 71 km for the time period 2004–2008 are shown: OSO (black), FTS (blue cross), MIPAS (200, green plus), MLS (red dots), SMR (V225, brown stars) and a priori (cyan dashed).

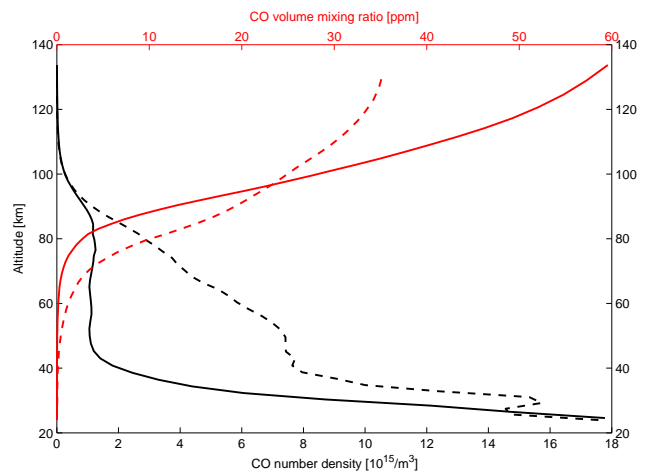


Fig. 11. The number density of CO (black) and the volume mixing ratio of CO (red) versus altitude. The data shown are the mean summer (solid) and mean winter (dashed) OSO a priori from WACCM. The main contribution to the column above 70 km originates from altitudes ≤ 100 km altitude.

5.3.1 ACE and MLS

The CO mixing ratios from OSO and the satellites MLS and ACE agree well and have a high correlation at all altitudes. Between 55 and 70 km the difference in mixing ratios between OSO and ACE and MLS is less than 15% (Fig. 12 and Table 4). The deviation between ACE and MLS, as seen in Fig. 12, has been reported earlier by Pumphrey et al. (2007) and Clerbaux et al. (2008). As seen in both Fig. 12 and

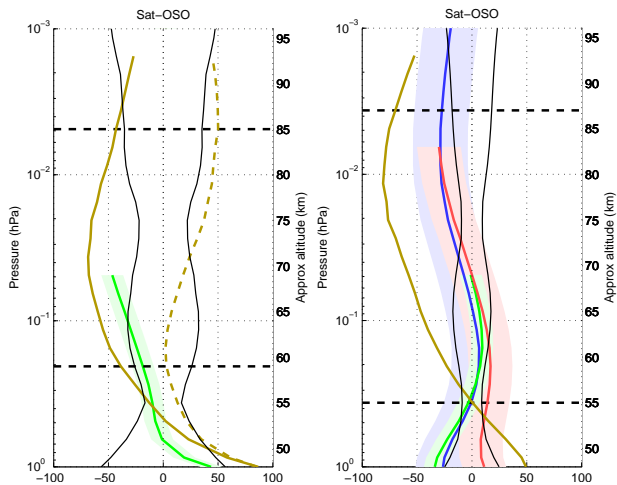


Fig. 12. Mean relative differences between satellites and OSO; (Left): the time period 2002–2004, MIPAS (12 + 13, green), SMR (V021, dashed brown) and SMR (V225, solid brown). (Right): the time period 2004–2008, FTS (blue), MIPAS (200, green), MLS (red) and SMR (V225, brown). The deviating lengths of the satellite profiles is explained by the different vertical coverage of the satellites. The shaded areas show the estimated systematic error of the different satellites. The vertical black lines are the estimated systematic errors of the OSO instrument, 2002–2004 the worst case systematic error is used due to baseline problems (see Sect. 4.2). The horizontal black dashed lines show the vertical limits of the OSO observations. The summer values are excluded.

Table 4 OSO has higher CO mixing ratios above 70 km compared to ACE and MLS leading to 25 % higher CO column values (> 71 km). The MLS column values are close to the OSO a priori since the upper limit of MLS is about 80 km and we use the a priori CO data for grid points outside the vertical range of the satellite (see Sect. 5.2).

5.3.2 MIPAS

MIPAS (200) shows only a small deviation in CO mixing ratios compared to OSO. MIPAS (12 + 13) does not show the same good agreement when compared to OSO, it has up to 50 % lower values than OSO above 55 km. MIPAS (12 + 13) and MIPAS (200) have the same vertical coverage though MIPAS (200) is slightly better vertically sampled (due to shorter integration time). Resulting vertical resolutions of retrieved profiles, however, are quite similar.

Up to March 2004 only MIPAS (12 + 13) data are available and after March 2004 only MIPAS (200) data. In this comparison we have no overlap between MIPAS (12 + 13) and the other satellites except a few collocations with SMR (021 + 225). Clerbaux et al. (2008) compared CO data from the beginning of 2004 from MIPAS (9 + 10) and ACE and found that the CO mixing ratios from MIPAS (9 + 10) is within ± 26 % of the ACE mixing ratios in the altitude range 55–70 km. The most probable reason for the deviation

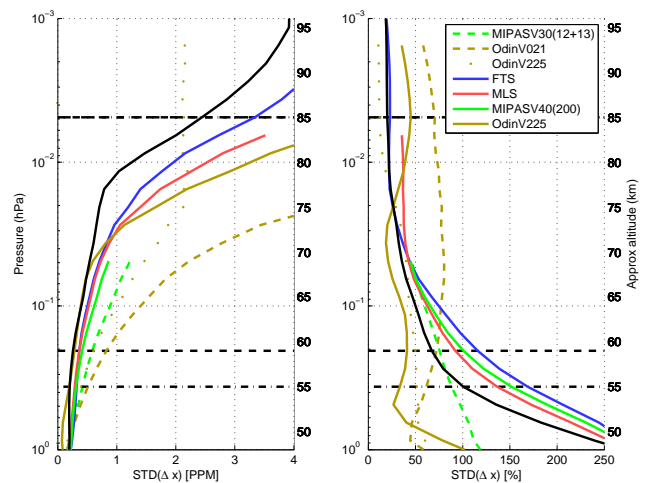


Fig. 13. The mean standard deviation between OSO and the satellites; absolute (left) and relative (right). MIPAS (12 + 13), SMR (v021), and the dotted SMR (v225) are from the time period 2002–2004. The vertical coverage of the satellites explains the deviating extension of the profiles. The horizontal black dashed lines show the vertical limits of the OSO observations. The dashed line at 60 km is the lower limit 2002–2004 and the dash-dotted line at 55 km is the lower limit 2004–2008. The black line is the root-sum of the average retrieval noise and the total forward model parameter variability of the OSO instrument. The summer values are excluded.

between OSO and MIPAS (12 + 13) can be the baseline features seen in the OSO spectra before 2004.

5.3.3 SMR

The two CO datasets of SMR deviate in different ways compared to the OSO data at 55–95 km. SMR (225) shows down to 65 % lower mixing ratios than OSO and SMR (021) shows up to 50 % higher mixing ratios (Fig. 12). A reason for the general discrepancy between SMR and OSO can be the few co-locations with OSO but this does not explain the difference between the two SMR versions. V021 is regarded to be the more accurate than v225. Comparisons between SMR (021 + 225) and ACE shows the same general discrepancy between v225 and v021 (not shown).

6 Summary and conclusions

Ground-based, frequency-switched measurements of mesospheric CO at 115 GHz from Onsala Space Observatory (57° N, 12° E) during the time period 2002–2008 are presented.

Signal-reference switching is the standard microwave observation method in order to reduce the effect of gain drift in the receiver system. A frequency-switched radiometer is an especially simple instrument since almost no moving parts are needed (except a hot load flag). The advantages with frequency-switching include also that both gain nonlinearity

Table 4. Statistics for 55 km, 63 km and for total columns > 71 km. *Mn (%)* the mean relative difference of CO between satellite and OSO (> 0 if the satellite reports more CO than OSO), *Std (%)* the mean standard deviations, *Corr* the mean correlation of CO between satellite and OSO, *total* the total number of co-located measurements, *days* the number of days with co-located measurements. The summer values are excluded.

	55 km			63 km			> 71 km			co-locations	
	Mn	Std	Corr	Mn	Std	Corr	Mn	Std	Corr	total	days
FTS	-1	169	0.82	4	82	0.89	-22	18	0.96	148	108
MIPAS (12 + 13)	-10	88	0.72	-30	63	0.73	-	-	-	1424	194
MIPAS (200)	-3	152	0.76	9	71	0.77	-	-	-	1842	180
MLS	14	136	0.81	14	68	0.86	-24	28	0.89	19250	506
SMR (v021) < 04	13	62	0.78	4	76	0.74	42	66	0.85	22	8
SMR (v225) < 04	-13	51	0.76	-55	45	0.72	-47	15	0.73	11	6
SMR (v225) > 04	1	33	0.82	-40	39	0.75	-68	32	0.35	14	8

and gain variations are almost canceled out and that no time is spent observing a reference load. Frequency-switching is very well suited for the observation of narrow transition lines as in the case of mesospheric CO at 115 GHz.

The Optimal Estimation Method, OEM, has been used to retrieve vertical CO profiles from the measured spectra. A thorough error analysis has been performed to investigate the systematic effects due to the uncertainties in the different parameters used in the measurement and retrieval process to give an as accurate error estimation as possible.

The OSO instrument has provided the longest time series of ground-based mesospheric CO measurements so far. The OSO data show the same general features as data from satellite instruments both in the annual cycle, characterized by high CO mixing ratios during winter and very low mixing ratios during summer, and in shorter time period events.

The OSO CO data have been compared to CO datasets from four satellite instruments; ACE-FTS (v2.2) on Scisat, MIPAS (V3O_CO_12 + 13 and V4O_CO_200) on Envisat, MLS (v3-3) on Aura and SMR (v225 and v021) on Odin.

A satellite measurement is assumed to be co-located with OSO if the measurement is done the same day and if the air at the tangent point of the satellite both is within a radius of 1500 km from OSO and deviates less than 20% in PV (potential vorticity) compared to the air above OSO.

During the time period 2004–2008 the averaged CO datasets retrieved by OSO and ACE, MLS and MIPAS (200) do not differ by more than 15% in the altitude range 55–70 km, which is within the combined systematic errors of the different instruments (see Fig. 12b).

The time period 2002–2004 MIPAS (12 + 13) shows up to 50% smaller mixing ratios compared to OSO. One reason for the observed difference between the OSO and MIPAS (12 + 13) mesospheric CO datasets can be due to baseline features seen in the OSO spectra before February 2004.

SMR (021 + 225) have very few co-located CO measurements with OSO. V225 shows up to 65% lower mixing ratios than OSO and the v021 measurements show up to 50% higher mixing ratios than OSO.

Above 70 km we compare the CO column values from OSO and the satellite sensors ACE, MLS and SMR. The OSO column values are about 25% higher than the values from both ACE and MLS. SMR (021) shows up to 65% higher column values than OSO. The MLS column values are close to the OSO a priori values since we use a priori information outside the vertical range of the satellite (the upper vertical limit for MLS is 80 km). SMR has very few co-located measurements with OSO.

The systematic error above 70 km is $\pm 25\%$ for ACE and $\pm 10\%$ for OSO. If the systematic errors for ACE and OSO are correctly estimated the mean true profile has to be in the range where the mean profiles of OSO and ACE (inclusive their systematic errors) overlaps. Since ACE shows 25% lower column values than OSO, this indicates that OSO has a positive bias of less than 10% above 70 km and that ACE has a negative bias of about 15–25% above 70 km (see Fig. 12b). Hoffmann et al. (2011) report an offset pattern when their ground-based instrument is compared to ACE and MLS, which is similar to the offset pattern we report when OSO is compared to the same satellites. Additional comparisons of upper mesospheric CO are needed to understand the reason for this observed offset between ground-based and satellite instruments.

Observation of mesospheric CO provides important information of the mesospheric dynamics. The satellite sensors which measure mesospheric CO today are not, to our knowledge, planned to be replaced when they stop functioning. Therefore, in a few years, ground-based instruments will be even more important than today. The CO transition at 115 GHz is suitable for ground-based studies of the upper atmosphere due to both that the lower atmosphere is fairly transparent, at this frequency, and that pressure broadening exceeds Doppler broadening as high as 70 km, making it possible to estimate vertical profiles up to this altitude and to estimate column values above.

The exact CO abundance in the upper mesosphere is still an open question. Further ground-based measurements at

115 GHz can be used as a low cost alternative to clarify this issue.

Acknowledgements. The Swedish Natural Science Research Council supported the maintenance and development of the OSO receiver system. We thank the teams behind HITRAN, JPL and WACCM for providing a priori information to the retrievals. We thank the community behind ARTS for software used in the retrieval process. We thank ECMWF for wind field data and the teams behind MLS/Aura, MIPAS/Envisat and ACE-FTS/SCISAT for providing the satellite CO datasets. The Atmospheric Chemistry Experiment (ACE), also known as SCISAT, is a Canadian-led mission mainly supported by the Canadian Space Agency and the Natural Sciences and Engineering Research Council of Canada. We also thank the Department of Earth and Space Sciences, Chalmers University of Technology for SMR/Odin CO data. Odin is a Swedish-led satellite project funded jointly by the Swedish National Space Board (SNSB), the Canadian Space Agency (CSA), the National Technology Agency of Finland (Tekes), the Centre National d'Etudes Spatiales (CNES) in France and the European Space Agency (ESA). We thank the laboratory and workshop of Onsala Space Observatory for keeping the OSO receiver up and running. Finally we thank the reviewers for their helpful comments on the manuscript.

Edited by: R. Sussmann

References

- Aellig, C., Kaempfer, N., and Hauchecorne, A.: Variability of mesospheric CO in the fall and winter as observed with ground-based microwave radiometry at 115 GHz, *J. Geophys. Res.*, 100, 14125–14130, doi:10.1029/95JD00984, 1995.
- Allen, D., Stanford, J., López-Valverde, M., Nakamura, N., Lary, D., Douglass, A., Cerniglia, M., Remedios, J., and Taylor, F.: Observations of middle atmosphere CO from the UARS ISAMS during the early northern winter 1991/92, *J. Atmos. Sci.*, 56, 563–583, doi:10.1175/1520-0469(1999)056<0563:OOMACF>2.0.CO;2, 1999.
- Baron, P., Ricaud, P., de La Noë, J., Eriksson, P., Merino, F., and Murtagh, D.: Studies for the Odin sub-millimetre radiometer: Retrieval methodology, *Can. J. Phys.*, 80, 341–356, doi:10.1139/P01-150, 2002.
- Bevilacqua, R., Stark, A., and Schwartz, P.: The variability of carbon monoxide in the terrestrial mesosphere as determined from ground-based observations of the $J = 1 \rightarrow 0$ emission line, *J. Geophys. Res.*, 90, 5777–5782, doi:10.1029/JD090iD03p05777, 1985.
- Borsdorff, T. and Sussmann, R.: On seasonality of stratomesospheric CO above midlatitudes: New insight from solar FTIR spectrometry at Zugspitze and Garmisch, *Geophys. Res. Lett.*, 36, 804, doi:10.1029/2009GL040056, 2009.
- Burrows, S., Martin, C., and Roberts, E.: High-latitude remote sensing of mesospheric wind speeds and carbon monoxide, *J. Geophys. Res.*, 112, 109, doi:10.1029/2006JD007993, 2007.
- Clancy, R., Muhleman, D., and Allen, M.: Seasonal variability of CO in the terrestrial mesosphere, *J. Geophys. Res.*, 89, 9673–9676, doi:10.1029/JD089iD06p09673, 1984.
- Clerbaux, C., George, M., Turquety, S., Walker, K. A., Barret, B., Bernath, P., Boone, C., Borsdorff, T., Cammas, J. P., Catoire, V., Coffey, M., Coheur, P.-F., Deeter, M., De Mazière, M., Drummond, J., Duchatelet, P., Dupuy, E., de Zafra, R., Eddounia, F., Edwards, D. P., Emmons, L., Funke, B., Gille, J., Griffith, D. W. T., Hannigan, J., Hase, F., Höpfner, M., Jones, N., Kagawa, A., Kasai, Y., Kramer, I., Le Flochmoën, E., Livesey, N. J., López-Puertas, M., Luo, M., Mahieu, E., Murtagh, D., Nédélec, P., Pazmino, A., Pumphrey, H., Ricaud, P., Rinsland, C. P., Robert, C., Schneider, M., Senten, C., Stiller, G., Strandberg, A., Strong, K., Sussmann, R., Thouret, V., Urban, J., and Wiacek, A.: CO measurements from the ACE-FTS satellite instrument: data analysis and validation using ground-based, airborne and spaceborne observations, *Atmos. Chem. Phys.*, 8, 2569–2594, doi:10.5194/acp-8-2569-2008, 2008.
- de Zafra, R. and Muscari, G.: CO as an important high-altitude tracer of dynamics in the polar stratosphere and mesosphere, *J. Geophys. Res.*, 109, D06105, doi:10.1029/2003JD004099, 2004.
- Dupuy, E., Urban, J., Ricaud, P., Le Flochmoën, É., Latié, N., Murtagh, D., De La Noë, J., El Amraoui, L., Eriksson, P., Forkman, P., Frisk, U., Jégou, F., Jiménez, C., and Olberg, M.: Stratospheric measurements of carbon monoxide with the Odin Sub-Millimetre Radiometer: Retrieval and first results, *Geophys. Res. Lett.*, 31, L20101, doi:10.1029/2004GL020558, 2004.
- Eriksson, P.: Analysis and comparison of two linear regularization methods for passive atmospheric observations, *J. Geophys. Res.*, 105, 18157–18167, doi:10.1029/2000JD900172, 2000.
- Eriksson, P., Jiménez, C., and Buehler, S. A.: Qpack, a tool for instrument simulation and retrieval work, *J. Quant. Spectrosc. Ra.*, 91, 47–64, doi:10.1016/j.jqsrt.2004.05.050, 2005.
- Eriksson, P., Buehler, S. A., Davis, C. P., Emde, C., and Lemke, O.: ARTS, the atmospheric radiative transfer simulator, Version 2, *J. Quant. Spectrosc. Ra.*, 112, 1551–1558, doi:10.1016/j.jqsrt.2011.03.001, 2011.
- Forkman, P., Eriksson, P., and Winnberg, A.: The 22 GHz Radio-astronomy receiver at Onsala Space Observatory, *J. Quant. Spectrosc. Ra.*, 77, 23–42, doi:10.1016/S0022-4073(02)00073-0, 2003a.
- Forkman, P., Eriksson, P., Winnberg, A., Garcia, R., and Kinnison, D.: Longest continuous ground-based measurements of mesospheric CO, *Geophys. Res. Lett.*, 30, 1532, doi:10.1029/2003GL016931, 2003b.
- Forkman, P., Eriksson, P., and Murtagh, D.: Observing the vertical branch of the mesospheric circulation at lat N60° using ground based measurements of CO and H₂O, *J. Geophys. Res.*, 110, 107, doi:10.1029/2004JD004916, 2005.
- Funke, B., López-Puertas, M., García-Comas, M., Stiller, G. P., von Clarmann, T., Höpfner, M., Glatthor, N., Grabowski, U., Kellmann, S., and Linden, A.: Carbon monoxide distributions from the upper troposphere to the mesosphere inferred from 4.7 μm non-local thermal equilibrium emissions measured by MIPAS on Envisat, *Atmos. Chem. Phys.*, 9, 2387–2411, doi:10.5194/acp-9-2387-2009, 2009.
- Garcia, R. R., Marsh, D. R., Kinnison, D. E., Boville, B. A., and Sassi, F.: Simulation of secular trends in the middle atmosphere, 1950–2003, *J. Geophys. Res.*, 112, D09301, doi:10.1029/2006JD007485, 2007.

- Hedin, A. E.: Extension of the MSIS thermosphere model into the middle and lower atmosphere, *J. Geophys. Res.*, 96, 1159–1172, doi:10.1029/90JA02125, 1991.
- Hoffmann, C. G., Raffalski, U., Palm, M., Funke, B., Golchert, S. H. W., Hochschild, G., and Notholt, J.: Observation of stratospheric CO above Kiruna with ground-based microwave radiometry – retrieval and satellite comparison, *Atmos. Meas. Tech.*, 4, 2389–2408, doi:10.5194/amt-4-2389-2011, 2011.
- Kasai, Y. J., Koshiro, T., Endo, M., Jones, N. B., and Murayama, Y.: Ground-based measurement of strato-mesospheric CO by a FTIR spectrometer over Poker Flat, Alaska, *Adv. Space Res.*, 35, 2024–2030, doi:10.1016/j.asr.2005.04.099, 2005.
- Lait, L.: An alternative form for potential vorticity, *J. Atmos. Sci.*, 51, 1754–1759, doi:10.1175/1520-0469(1994)051<1754:AAFFPV>2.0.CO;2, 1994.
- Lopez-Puertas, M., Lopez-Valverde, M., Garcia, R., and Roble, R.: A review of CO₂ and CO abundances in the middle atmosphere, *Geoph. Monog.*, 123, 83–100, doi:10.1029/GM123p0083, 2000.
- Marks, C. and Rodgers, C.: A retrieval method for atmospheric composition from limb emission measurements, *J. Geophys. Res.*, 98, 14939–14953, doi:10.1029/93JD01195, 1993.
- Melsheimer, C., Verdes, C., Buehler, S. A., Emde, C., Eriksson, P., Feist, D. G., Ichizawa, S., John, V. O., Kasai, Y., Kopp, G., Koulev, N., Kuhn, T., Lemke, O., Ochiai, S., Schreier, F., Sreerekha, T. R., Suzuki, M., Takahashi, C., Tsujimaru, S., and Urban, J.: Intercomparison of general purpose clear sky atmospheric radiative transfer models for the millimeter/submillimeter spectral range, *Radio Sci.*, 40, RS1007, doi:10.1029/2004RS003110, 2005.
- Pickett, H., Poynter, R., Cohen, E., Delitsky, M., Pearson, J., and Müller, H.: Submillimeter, millimeter, and microwave spectral line catalog, *J. Quant. Spectrosc. Ra.*, 60, 883–890, doi:10.1016/S0022-4073(98)00091-0, 1998.
- Pumphrey, H. C., Filipiak, M., Livesey, N., Schwartz, M., Boone, C., Walker, K., Bernath, P., Ricaud, P., Barret, B., Clerbaux, C., Jarnot, R., Manney, G., and Waters, J.: Validation of middle-atmosphere carbon monoxide retrievals from MLS on Aura, *J. Geophys. Res.*, 112, D24S38, doi:10.1029/2007JD008723, 2007.
- Rodgers, C. D.: Inverse methods for atmospheric sounding: Theory and practice, World Scientific, Singapore, 2000.
- Rodgers, C. D. and Connor, B.: Intercomparison of remote sounding instruments, *J. Geophys. Res.*, 108, 4116, doi:10.1029/2002JD002299, 2003.
- Rohlfs, K. and Wilson, T. L.: Tools of Radio Astronomy, Springer-Verlag, Berlin, 2008.
- Rothman, L., Barbe, A., Chris Benner, D., Brown, L., Camy-Peyret, C., Carleer, M., Chance, K., Clerbaux, C., Dana, V., Devi, V., Devic, V., Fayt, A., Flaudi, J., Gamachej, R., Goldman, A., Jacquemart, D., Jucks, K., Lafferty, W., Mandin, J., Massie, S., Nemtchinov, V., Newnham, D., Perrin, A., Rinsland, C., Schroeder, J., Smith, K., Smith, M., Tang, K., Toth, R., Vander Auwera, J., Varanasi, P., and Yoshino, K.: The HITRAN molecular spectroscopic database: edition of 2000 including updates through 2001, *J. Quant. Spectrosc. Ra.*, 82, 5–44, doi:10.1016/S0022-4073(03)00146-8, 2003.
- Velazco, V., Wood, S. W., Sinnhuber, M., Kramer, I., Jones, N. B., Kasai, Y., Notholt, J., Warneke, T., Blumenstock, T., Hase, F., Murcray, F. J., and Schrems, O.: Annual variation of strato-mesospheric carbon monoxide measured by ground-based Fourier transform infrared spectrometry, *Atmos. Chem. Phys.*, 7, 1305–1312, doi:10.5194/acp-7-1305-2007, 2007.
- Waters, J., Wilson, W., and Shimabukuro, F.: Microwave measurement of mesospheric carbon monoxide, *Science*, 191, 1174, doi:10.1126/science.191.4232.1174, 1976.